Materials Today Physics 35 (2023) 101102

Contents lists available at ScienceDirect

Materials Today Physics

journal homepage: www.journals.elsevier.com/materials-today-physics

One-step precise machining of terahertz microstructures on chip-scale lithium niobate via laser dispersion engineering

Xu Zhou [a,b], Yao Lu [a,b,**], Haibo Liu [c], Qiang Wu [a,b,*], Xitan Xu [a,b], Lu Chen [a,b], Zhixuan Li [a,b], Rui Wang [c], Jin Guo [c], Jingjun Xu [a,b]

[a] Key Laboratory of Weak-Light Nonlinear Photonics, Ministry of Education, TEDA Institute of Applied Physics and School of Physics, Nankai University, Tianjin, 300457, China

[b] Shenzhen Research Institute of Nankai University, Shenzhen, Guangdong, 518083, China

[c] State Key Laboratory of Laser Interaction with Matter, Changchun Institute of Optics, Fine Mechanics and Physics, Chinese Academy of Sciences, Changchun, 130033, China

A B S T R A C T

Chip-scale lithium niobate (LN) yields a competitive candidate for terahertz (THz) on-chip communications, which could enable high-rate data transmission, non-invasive biosensing, and cloud-based technologies. However, it remains a key challenge to reach such goals to fabricate functional millimeter-scale crack-free THz microstructures on chip-scale LN, especially for industrial use. Here, we propose a one-step crack-free microstructure fabrication approach using dispersion-engineered femtosecond laser pulses without involving any postprocessing method. By laser dispersion engineering, the fabricated one-dimensional photonic crystal can improve the THz transmittance by about 5.8 times compared to the general case. This achievement is based on a thorough investigation into the influence of femtosecond laser temporal dispersion on the lithium niobite machining process. Our findings may further promote the development and industrial applications of LN-based photonics and optoelectronics, especially for chip-scale THz devices, as well as offer insights into the realization of precision machining of other forms of hard and brittle materials.

1. Introduction

Terahertz (THz) technologies have received extensive attention due to its attractive prospects in the fields of wireless communications [1,2], sensing [3], non-invasive imaging [4,5], and signal processing [6,7]. A key step to popularize THz devices is to integrate many functional components on a chip. As a powerful candidate, lithium niobate ($LiNbO_3$, LN) crystal shows excellent properties for full-band photonics integration including THz band [8–11], where extensive applications are shown in nonlinear optics [10–12], integrated quantum photonics [10,11], and topological photonics [9,10,13]. Based on the LN platform, the generation [14–16] and material detection [17–19] of terahertz waves have been realized. However, the high-efficiency and high-precision LN processing remains a bottleneck towards millimeter-to-centimeter-scale applications of THz on-chip integration.

Compared with other typical high-precision processing methods for LN, such as dry etching [20], chemical mechanical polishing [21], and focused ion beam milling [22], femtosecond laser (fs-laser) micromachining has unique advantages such as high efficiency, flexibility, low-cost, and 3D fabrication [23,24]. Especially in the THz band with a submicrometer-scale wavelength, microstructures with dimensions from millimeters to centimeters are required, further highlighting the preponderance of fs-laser fabricating THz functional devices on LN chips. Although fs-laser micromachining of LN has made some achievements [25–32] and fabricated some on-chip integrated photonic devices, such as beam splitters [33], waveguide arrays [34], frequency converters [35], electro-optic modulators [36], and microresonators [37]. There is a conflict between efficiency and precision. As a typically hard and brittle material, the fragmentations and cracks of the structured edges in fs-laser processing LN will cause serious THz transmission loss, which makes it very challenge to prepare microstructured LN for industrial applications.

Precise control of the light-matter interaction process during femtosecond laser processing is a beneficial way to improve processing quality. In recent decades, shaped fs-laser pulses have been found as an effective way to process some dielectrics with a better quality [38–40],

* Corresponding author. Key Laboratory of Weak-Light Nonlinear Photonics, Ministry of Education, TEDA Institute of Applied Physics and School of Physics, Nankai University, Tianjin, 300457, China.

** Corresponding author. Key Laboratory of Weak-Light Nonlinear Photonics, Ministry of Education, TEDA Institute of Applied Physics and School of Physics, Nankai University, Tianjin, 300457, China.

E-mail addresses: yaolu@nankai.edu.cn (Y. Lu), wuqiang@nankai.edu.cn (Q. Wu).

https://doi.org/10.1016/j.mtphys.2023.101102

Received 17 March 2023; Received in revised form 10 April 2023; Accepted 27 April 2023

Available online 28 April 2023

while the feasibility of efficient machining of the crack-free microstructured LN wafer that aims to further develop THz on-chip integration remains unknown.

In this article, we propose a novel one-step approach to prepare crack-free micromachining of LN crystals through temporally shaped fs-laser pulses, which optimizes the balance between high efficiency and high precision. To demonstrate the versatility of this approach, identical one-dimensional Bragg photonic crystals are drilled on the same LN wafers using original and shaped pulses. As a result, when THz waves are excited in photonic crystals via pump-probe techniques, a noticeable improvement of the THz wave transmission associated with the shaped pulse is demonstrated. Besides, we experimentally investigate the relationship between crack formation with multi-order dispersion, including second-order and third-order dispersion, etc. A mechanism of competition between ultrafast ablation and thermal effects is finally proposed to explain the dispersion-related effects.

2. Results and discussion

2.1. Efficient high-quality micromachining LN through dispersion engineering

Temporal dispersion of femtosecond laser pulses exerts significant influence on the light-matter interaction process by broadening the pulse duration and distorting the pulse waveform. However, it still remains a challenge to fully control the transient light-matter interaction through flexible controlling the pulse dispersion. Generally, the compressor fails to completely cancel the multi-order temporal dispersion in a chirped pulse amplification system [41,42], even though the second- and third-order dispersion in the amplifier can be compensated to some extent [41,43]. Therefore, original fs-laser pulses from a commercial amplifier are the combinations of multi-order dispersion, especially second-order dispersion (group delay dispersion, GDD) and third-order dispersion (TOD). It is the different-orders of the temporal dispersion of the laser pulse that caused the cracks and broken edges on LN crystal during the laser micromachining process, as shown in Fig. 1 (a).

In the experiment, the LN wafers are irradiated by regeneratively amplified femtosecond laser pulses with a center wavelength of 800 nm and a repetition rate of 1 kHz. The experimental setup is shown in Fig. 1 (b). The temporal dispersion is modulated by a 4*f* pulse shaping system, and the MIIPS system plays the role of measurement and feedback. Notably, the pulse passes through some optical element of the processing system before it reaches the surface of the sample, which will introduce GDD of about 1300 fs^2, and it is not measured by the MIIPS system. The original dispersive pulse also passes through the shaper, while the shaper performs neither dispersion compensation nor additional dispersion. We fabricated some single-point ablations on a *z*-cut LN wafer with fluence of 9.4 kJ/m^2 original dispersive pulses (with a duration of 130 fs), GDD pulses (9000 fs^2), TOD pulses (5×10^6 fs^3), and dispersion-free pulses (with a duration of 90 fs), as shown in Fig. 1(a). For the original dispersive pulses, here appear plenty of different structural defects including both surface cracks (marked in red) and subsurface cracks (highlighted in blue). When using GDD pulses, namely chirped pulses, arc subsurface cracks are more likely to appear. In turn, straight surface cracks and broken edges are formed easier when TOD

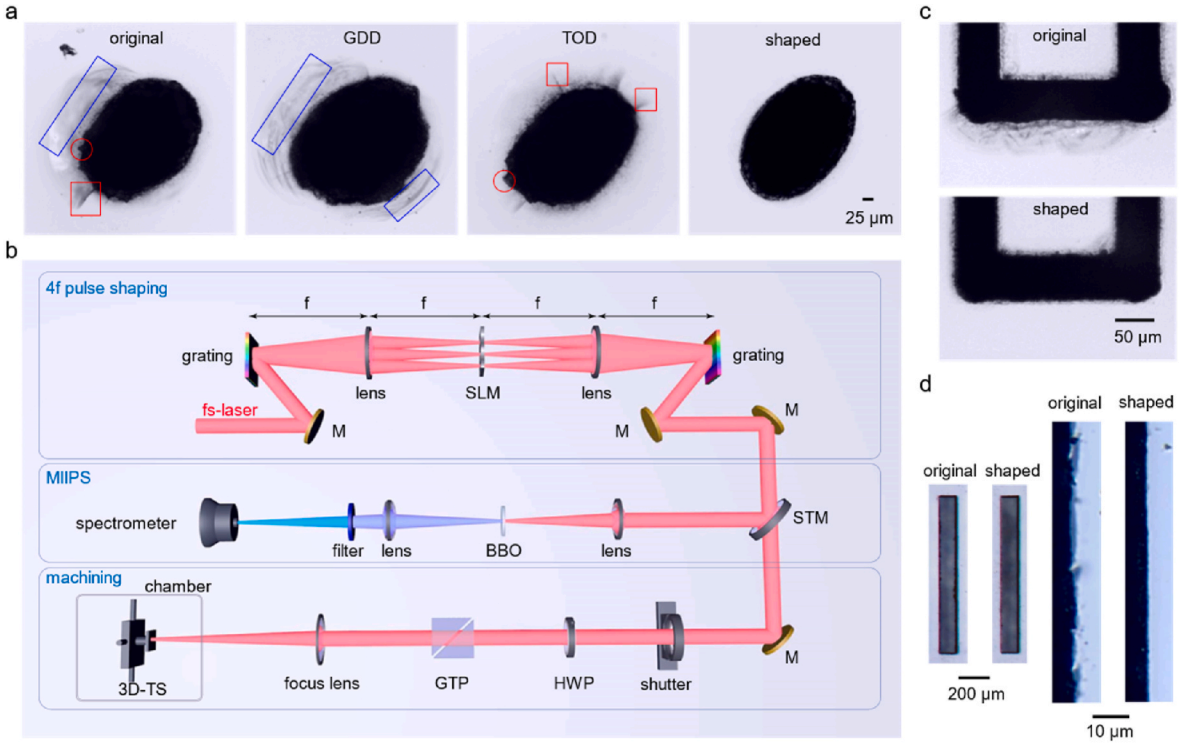

Fig. 1. Efficient high-quality micromachining LN through dispersion engineering. (a) Optical microscopy image of the ablation holes obtained using femtosecond laser pulses with different dispersion. From left to right: Surface ablation by original dispersive pulses from a regeneratively amplified femtosecond laser, GDD (9000 fs^2) pulses, TOD (5×10^6 fs^3) pulses and shaped dispersion-free pulses. Blue rectangles highlight some subsurface cracks, while red rectangles and red circles denote surface cracks and broken edges, respectively. Each spot was exposed to 1000 temporal-shaped pulses with the same peak fluence of 9.4 kJ/m^2. (b) Schematic diagram of the pulse-shaping machining system. Up: Schemes of 4*f* pulse shaping system, which consists of symmetrical gratings and lenses, and a spatial light modulator (SLM). M: mirrors. Middle: Schemes of MIIPS system, the spectral phase is characterized by MIIPS, STM: semi-transparent mirror. Down: Schemes of the fs-laser processing system. HWP: half-wavelength plate; GTP: Glan-Taylor polarizer; 3D-TS: three-dimension translation stage. Focus lens: 50 cm cemented achromatic double lens or objective (tight focus, NA = 0.25, 10 ×) (c) Micrograph of line ablation of LN wafer under the condition of tight focus at 7.0 mW by original dispersive pulses (up) and shaped dispersion-free pulses (down). (d) Rectangular air slots drilled on 50 μm LN crystal (coated with a 2 μm SiO_2 film) fabricated by dispersive pulses and dispersion-free pulses at 6.7 mW, as well as the air slot edges of the sample.

pulses are applied. Uneven energy distribution of the beam can contribute to cracks forming along the long axis of the ellipse. Additionally, there may be cracks that appear in random directions. Notably, the ablation holes fabricated by dispersion-free pulses have smooth boundaries and without any cracks.

To showcase the potential and universality of the temporal dispersion engineering, line ablation and drilling are performed on *x*-cut LN samples using different pulses focused by a microscope objective (10 ×, NA = 0.25). Fig. 1(c) depicts the micrographs of the surface morphologies after ablation with original dispersive pulses and shaped dispersion-free pulses. Compared to the dispersion-free pulses, dispersive pulses induce significant subsurface arc cracks with a range of 40 μm and corner defects, which means that neither the orientation of the LN crystal nor the way of focusing will affect the process of dispersion-controlled crack growth. In terms of line roughness, the maximum profile height of the transverse and longitudinal processing lines has been reduced from 5.7 μm and 12.1 μm to 2.8 μm and 4.0 μm, respectively. In particular, corners are more susceptible to cracks and defects because of the deceleration effect of the translation stage in the endpoint. This effect results in the overlapping of multiple pulses, which increases the incubation effect. The optimization of the stepper motor speed at the corners is anticipated to enhance the processing quality and make it more suitable for complex situations, such as curved processing.

Rectangular air slots are further drilled on a 50 μm thick LN wafer (double-side coated with 2 μm SiO_2 layers), which is commonly applied in THz photonics, using dispersive and shaped dispersion-free pulses, respectively (Fig. 1(d)). First, shaped fs-laser pulses are focused on the surface and the LN wafer is then moved with the translation stage along the shape of the slot. After that, the focal point is shifted in the sample depth by 8 μm and the previous process is repeated until the slot is drilled. To remove nanoparticles attached to the surface, the ablated LN wafer is soaked in hydrofluoric acid. Using 6.7 mW power, a scanning speed of 0.3 mm/s, and a 10 × objective lens for focusing processing, the diameter of ablation and its depth are approximately 50 μm and 8 μm, respectively. As Fig. 1(d) shows, there is a big contrast in edge smoothness for shaped dispersion-free pulses and dispersive pulses, especially in the magnified graph revealing the edge details, in which the maximum profile height of the edge has been reduced from 3 μm to submicron scales.

Overall, the above results demonstrate that the use of dispersion-free pulses significantly improves the quality of micromachining regardless of the crystal tangential and focusing conditions, and the technique is compatible with other post-processing routes. A key point to remember is that it only takes tens of seconds to drill a 1 mm long, 0.1 mm wide, and 50 μm thick air slot. By contrast, dry etching or focused ion beam milling can take tens of hours or more. Notably, the resolution of our method depends on the focus parameter, and the best resolution could achieve 3 μm when employing a 10x objective lens, which could machine very fine structures for THz waves. With a scanning speed of 0.3–0.5 mm/s, a millimeter microstructure can be made only in an hour. For this method, the ablation depth can be rigorously controlled by setting axial scanning. With a focus depth of about 5 μm, we can either ablated a 5 μm-deep structure by single scan or drilled the whole 50 μm wafer as what we did.

2.2. Low-loss THz-photonic crystals fabricated by dispersion-free fs-laser pulses

As one of the best carriers for the development of THz chips, LN crystals have extensive application prospects in the fields of THz signal generation, guiding, manipulation, and detection [8,10]. However, the loss of THz signals due to both the material absorption and structural imperfections in the transmission greatly affects the performance of LN chips.

In order to further showcase the improvement of the micromachining quality by the dispersion-free pulses, an identical photonic crystal is fabricated by two kinds of pulses on the same LN wafer and tested for its ability to transmit THz signals. Seven rectangular air slots with a length of 1 mm, a width of 0.1 mm, and a spacing of 0.1 mm are drilled on a 30 μm *x*-cut LN wafer using 7.0 mW dispersive and shaped dispersion-free pulses, respectively. After that, the sample is divided into three zones that are generation, structure, and transmission regions, as shown in Fig. 2(a). The THz waves vibrating along the optical axis are excited in the generation region, by line-focused fs-laser pulses. The pump-probe technology is finally used to detect the THz wave propagation through the photonic crystals fabricated on the LN sample.

A three-dimensional (*x*, *y*, *t*) THz wave intensity distribution can be obtained by means of the pump-probe system with a delay line. When needed, the data pertaining to the time period during which THz waves propagate in the corresponding area is selected for processing. Integrating the *y*-component and performing the Fourier transform on the *x*- and *t*-components, the dispersion curves of the structure region and transmission region can be collected, as shown in Fig. 2(b). In particular, the signals in the structure region of the photonic crystal fabricated with dispersive pulses are almost entirely merged due to their scattering by the structure. In contrast, it observes the propagation signal in the structure region of the photonic crystal fabricated by dispersion-free pulses. Besides, there is a clear contrast in the transmission region, especially in the part where the frequency is greater than 0.4 THz. To quantitatively compare the transmission intensities of the transmission area, the position components are afterward integrated (see Fig. 2(c)). The intensities of the THz waves in the generation region can be regarded as equal; therefore, there is a huge increase in transmittance over the full frequency range. Since the high-frequency THz waves are more likely to be absorbed and scattered by defects in the cracked edges, the increase in transmittance is more obvious in the high-frequency band. Especially, the transmittance at 0.59 THz after the wave propagation through a photonic crystal produced by the dispersion-free pulses is magnified by about 5.8 times as compared to that treated with the dispersive pulses. Thus, the above results are of great importance for the fields of THz sensing and detection on LN.

2.3. Dependence of cracks/fragmentations on the temporal dispersion of fs-laser pulses

In order to further clarify the internal relationship between pulse dispersion and cracks, the effects of GDD and TOD on processing are investigated in detail, respectively. The probability of crack initiation under specific GDD and fluences is summarized by an intuitive distribution diagram in Fig. 3(a), in which also highlights the ablation morphology with specific fluences and GDD pulses. The “crack-free” and the “crack-prone” regions are represented using blue and red undertones, respectively. As can be seen, the ablation holes fabricated using dispersion-free pulses (GDD = 0 fs^2) have smooth edges, even at the high pulse fluence F = 11.0 kJ/m^2. Besides, cracks are hardly induced at the pulse fluence F = 7.8 kJ/m^2, which is slightly above the ablation threshold (around 7.0 kJ/m^2) of LN. As the fluence or GDD increases, the area of the subsurface cracks becomes noticeably larger. The worse surface cracks are induced eventually when the fluence F = 11.0 kJ/m^2 and GDD = 9000 fs^2. Overall, the formation of cracks is significantly suppressed when the dispersion value is around the left side of zero. The asymmetry between the negative and positive GDD originates from the transmission dispersion of the optical path, mentioned in the introduction of the experimental systems. Therefore, in practical applications, both the dispersion from the amplifier itself and the transmission dispersion in the optical path are of great significance.

Similarly, the probability of crack initiation under specific TOD and fluence is summarized in Fig. 3(b). This figure is axisymmetric, since the TOD that can be introduced from processing system is at a very low level. Different from the symmetry waveform of GDD, the positive TOD pulse is characterized by a strong initial pulse followed by a decaying pulse sequence; in contrast, the negative TOD causes a series of pre-

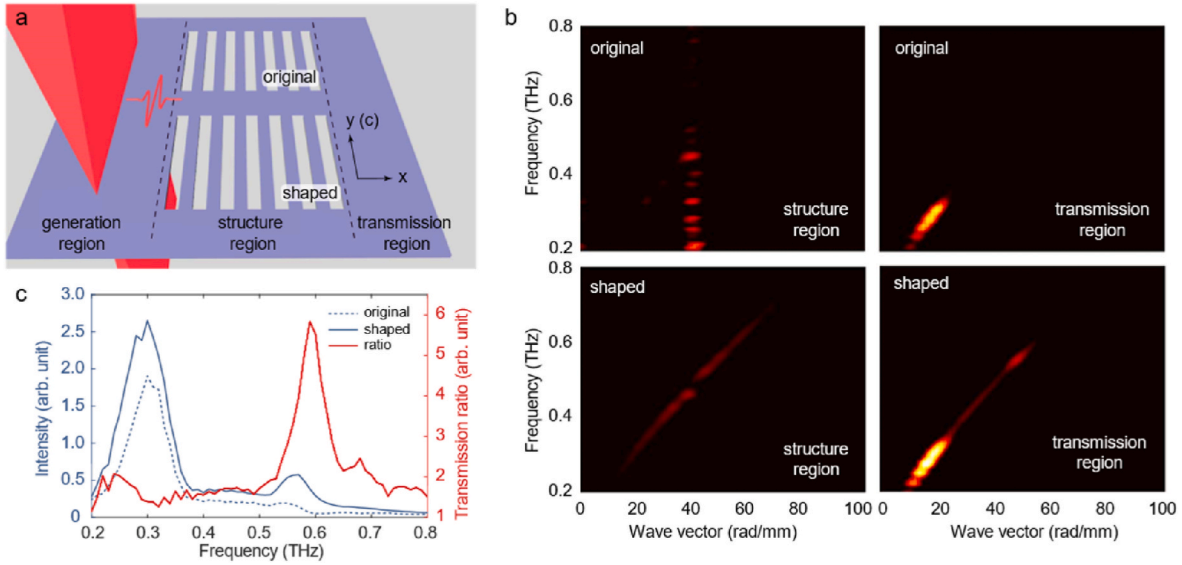

Fig. 2. Pumping and detection of terahertz phonon polariton on LN chips. (a) Schematic diagram of generation and propagation of THz waves in photonic crystals fabricated using dispersive and shaped dispersion-free pulses. (b) Dispersion curves in the structure and transmission regions. The first and second rows correspond to dispersive and shaped dispersion-free pulses, respectively. The images from left to right correspond to structure and transmission regions. (c) Quantitative comparison of transmitted intensity. The left axis refers to the spectrum intensity in the transmission region. The right axis is attributed to the ratio of the above two signal intensities.

pulses. Some broken edges already exist around the ablation hole at the TOD equal to $\pm 5 \times 10^5$ fs^3, while the pulse just possesses an asymmetric shape and no obvious sub-pulses has been excited. It is worth emphasizing that the pulse fluence is at a low level at this time, being just beyond the ablation threshold. As the absolute value of TOD increases, lots of surface cracks and subsurface cracks begin to appear in the vicinity of the ablation holes, especially when TOD equal to $\pm 5 \times 10^6$ fs^3.

When the TOD is larger than 5×10^5 fs^3, the pulse exhibits the properties of multiple pulses in addition to the asymmetric characteristics. Moreover, there is no obvious difference in crack formation between the positive and negative TOD pulses. Therefore, to study the effect of multiple pulses, shaped multiple pulses are generated based on the delay principle of the first-order dispersion to ablate LN, as shown in Fig. 3(c). All the sub-pulses are dispersion-free. Since the peak field strength of the multiple pulses is reduced, the ablation threshold is significantly increased. Specifically, double pulses and triple pulses are used to ablate the LN at 13.4 kJ/m^2, respectively, wherein the delay times of double pulses are 1 ps and 4 ps and that of triple pulses is 1 ps. Besides, mainly straight surface cracks are induced when using the multiple pulses with the fluence around the ablation threshold. This result coincides with the fact that TOD pulses are more likely to initiate surface cracks.

The above results demonstrate that temporal dispersion exerts a larger influence on crack formation than pulse fluence during fs-laser processing of LN. The GDD is easy to be introduced at the processing system, and the higher-order dispersion including TOD generally exists in original pulses from commercial femtosecond laser amplifiers. Different dispersion is easy to induce different shapes of cracks. Especially when using TOD and multiple pulses, shallower ablation and stronger thermal action are more likely to induce surface cracks and fragmentations. Therefore, the excessive pursuit of pulse fluence and the neglect of temporal dispersion may limit the development of high-power femtosecond laser processing for hard and brittle materials. Meanwhile, low-power laser modification with post-processing technology significantly limited the machining efficiency.

2.4. Mechanisms of the crack formation in hard and brittle materials caused by dispersion of fs-laser pulses

Generally, cracks in hard and brittle materials are induced by stress that is generated during fs-laser machining. Nevertheless, the reduction of stress via controlling the laser parameters such as fluence and pulse number is inevitably accompanied by sacrificing processing efficiency [44–46]. This is because the light-matter interaction cannot be precisely controlled, thereby hindering high-efficiency crack-free precision machining. However, temporal dispersion, which can be modulated arbitrarily through the pulse shaping technique, could exert a remarkable influence on the transient light-matter interaction by altering the duration and waveform of the pulses.

Fig. 4(a) depicts the schematic of some important physical processes in crack formation. In wide bandgap materials, fs-laser pulses can excite plenty of carriers through multi-photon ionization and avalanche ionization [47]. As a result, the pulse energy gets transferred to the lattice, leading to the formation of the plasma at a picosecond time scale [48, 49]. Within a few nanoseconds, the shock wave begins to spread out of the focal volume [45,50]. The shock wave originates from the thermal motion of plasma particles and electrons so that the thermal pressure is induced. It is proportional to the temperature of the plasma and can be several orders of magnitude of a million-atmosphere pressure [45]. The accumulation of stress, in turn, causes cracking on the edge of the ablation area. Besides, thanks to the high peak intensity and strong nonlinearity of fs-laser pulses, ultrafast material removal, including Coulomb explosion and phase explosion on the time scale of picoseconds, will occur at the picosecond scale [51]. It can take away the energy accumulated in the material and inhibit the generation of thermal cracks. Therefore, the formation of cracks can be considered a result of the competition between ultrafast ablation and conventional thermal effects.

As shown in Fig. 4(a), through broadening duration and distorting waveform, dispersion reduces peak intensity and inhibits nonlinearity and ultrafast removal. Besides, dispersion enables the carriers to be heated for a long time, forming a higher-temperature plasma and finally promoting the generation of cracks. Numerous studies have demonstrated that, when the pulse fluence is sufficient to ablate various materials, the use of dispersive pulses can result in the formation of higher

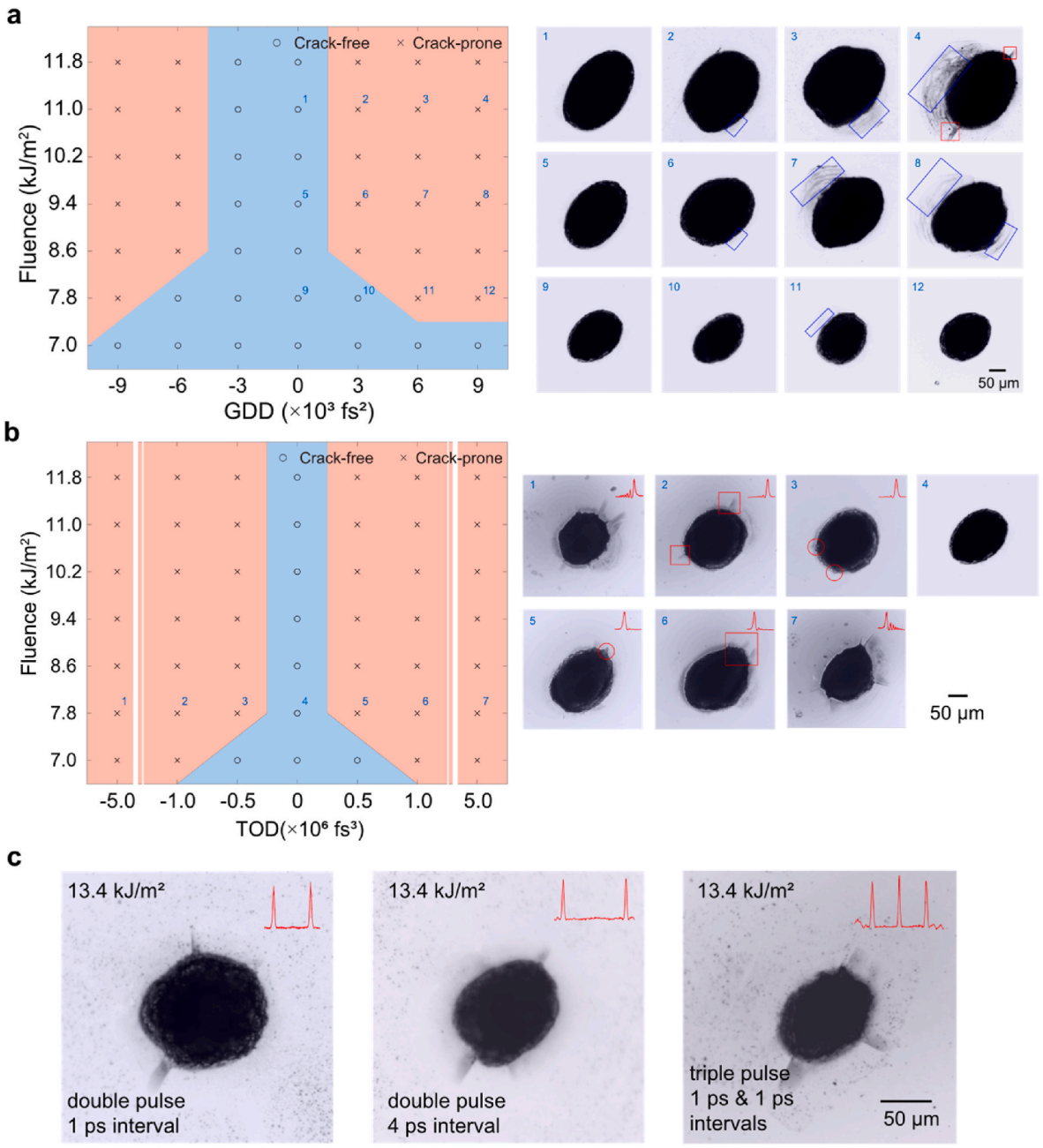

Fig. 3. Influence of multi-order dispersion and multiple pulses on the process of fs-laser ablation of LN. The optical axis of LN is perpendicular to the surface. Each spot was exposed to 1000 temporal-shaped pulses. (a, b) Probability distributions of crack formation with different (a) GDD and (b) TOD pulses. The circle in the blue area represents ablation without cracks, and the crosses in the orange region denote cracks that are easily induced during ablation. Some optical microscopy images of ablation with specific parameters are shown on the right. Blue rectangles highlight some subsurface cracks, while red rectangles and red circles denote surface cracks and broken edges, respectively. (c) The images of the LN ablated by multiple pulses (shaped double pulses and triple pulses, and the delay time of sub-pulses is indicated) at 13.4 kJ/m^2. All the sub-pulses are dispersion-free. Schematic diagrams of the waveform of the TOD and multiple pulses are illustrated in the upper right corner.

temperature plasma compared to dispersion-free pulses with identical fluence [52–54]. In summary, dispersive pulses can enhance conventional thermal effects during laser ablation. By contrast, only increasing the pulse fluence promotes both ultrafast ablation and thermal effects. However, due to the above-mentioned competition, it does not significantly impact the thermal effects, as compared to the influence of dispersion itself. Therefore, the contribution from the temporal dispersion to the crack formation is greater than that from the fluence.

For 800 nm fs-laser pulse, the band gap of LN is about 4 eV, so three photon ionization is dominant nonlinear effect, which is proportional to the cube of the pulse intensity I^3. Therefore, the nonlinear effect of the pulse can be quantitatively compared by integrating I^3. Figs. 4(b) and (c) shows the ratio of integral of pulses with the same fluence but different dispersion, taking the 90 fs dispersion-free pulse as a reference. The solid line means the theoretical curve, and the scattered points are measured by the MIIPS system. As Figs. 4(b) and (c) shows, the value of nonlinear integral decreases exponentially with the increase of dispersion. Besides, the measured value fits the theoretical value well, and there is a small amount of systematic error. As shown in Figs. 3 and 4, whether GDD or TOD, when the nonlinear integral value drops by about half, it corresponds to the turning point of crack formation, which is the eigenvalue associated with the properties of the material. As for shaped double

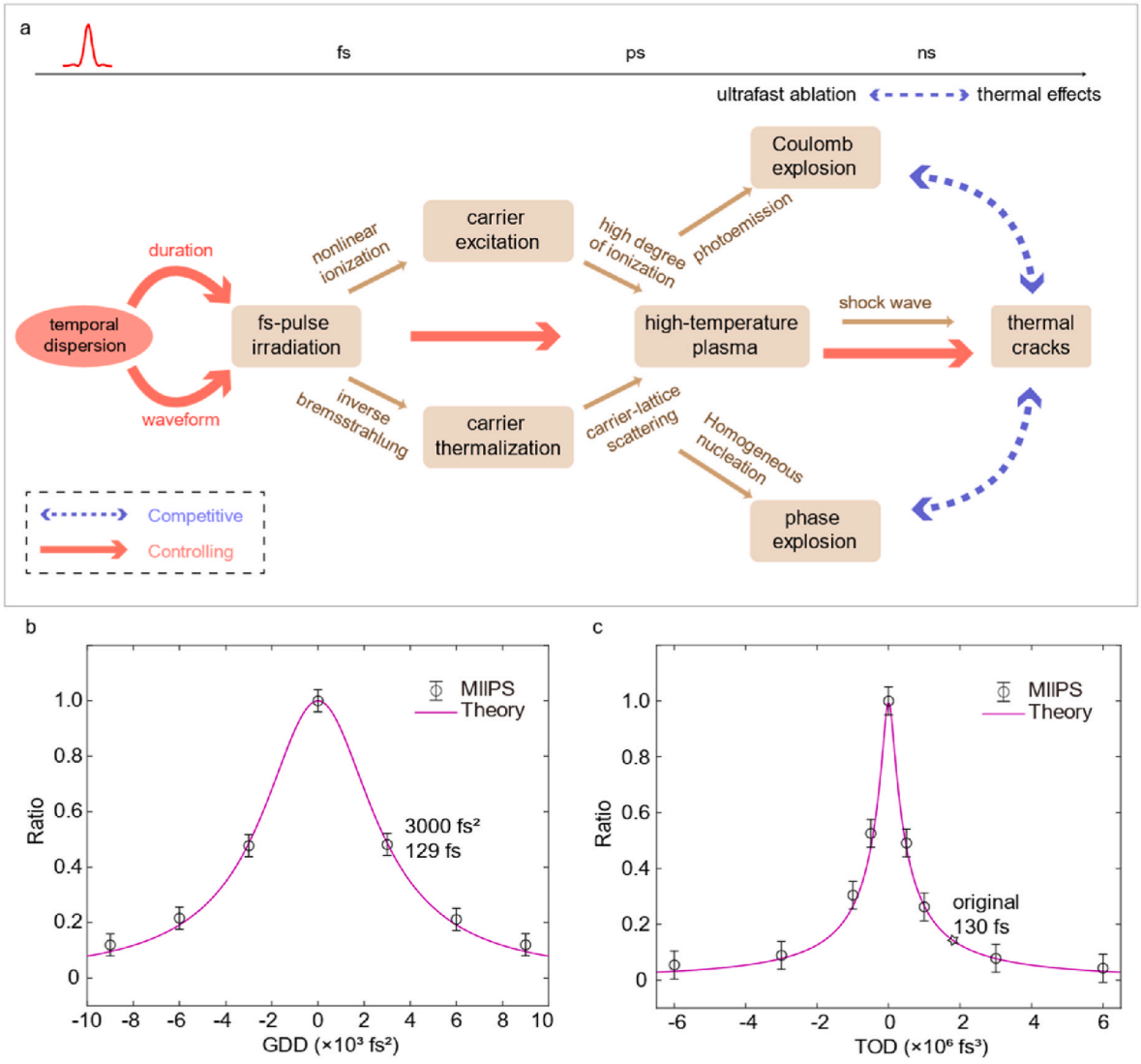

Fig. 4. Mechanisms of the crack formation in hard and brittle materials caused by dispersion of fs-laser pulses. (a)Schematic representation of the competitive relationship leading to crack formation in hard and brittle dielectric materials. Rounded rectangles denote important physical processes in crack formation. Arrows show the main relations between various processes. Blue dotted double arrows indicate the competitive relationship. Red arrows display the controlling relationship from temporal dispersion. (b, c) The ratio of the time integral of the cubed pulse intensity (corresponding to the three-photon nonlinearity) with different (b) GDD and (c) TOD, taking the 90 fs dispersion-free pulse as a reference. The solid line means the theoretical curve, and the scattered points are measured by the MIIPS system.

pulses and triple pulses, their nonlinear integral values are reduced to 0.25 and 0.11 times in theory. Moreover, the nonlinear integral value of the original dispersive pulse measured by MIIPS is around 0.14, which is marked in Fig. 4(c). Therefore, both the shaping multiple pulses and the original dispersive pulses are in the crack-prone zone.

It's notably that the duration of GDD pulses (90 fs, GDD = 3000 fs^2) and original dispersive pulses is equivalent, however, the nonlinear intensity is quite different (Figs. 4(b) and (c)). Besides, as follows from Figs. 1(a) ($F = 9.4$ kJ/m^2, original dispersive) and 3(a6) ($F = 9.4$ kJ/m^2, GDD = 3000 fs^2), the original pulses with higher-order dispersion are more likely to induce large-area cracks than GDD pulses with the same duration and fluence. That is, duration is not the only decisive factor caused by dispersion-controlled cracks. Actually, the higher-order dispersion, especially TOD, exerts a greater influence on the waveform, which usually deteriorates the micromachining quality and precision more through the waveform deformation.

3. Conclusion

In summary, our work provides a novel one-step approach to achieving high-efficiency crack-free fabrication of chip-scale lithium niobate, which benefits the progress of THz on-chip technologies. Special attention is paid to the investigation of the dependence of crack formation on temporal dispersion. In particular, temporal dispersion, is demonstrated to show remarkable influence on crack formation more than pulse fluence during fs-laser processing of $LiNbO_3$. By flexibly controlling the pulse dispersion, we eliminate the cracks that originate from the reduction of nonlinear effect and the enhancement of conventional thermal effects. We also show that any changes in both duration and waveform caused by the temporal dispersion will accelerate the crack growth by modulating light-matter interactions. Compared to the original dispersive pulses, the shaped dispersion-free pulses allow one to significantly improve the edge quality of micromachined $LiNbO_3$. The results also show that microstructures processed by dispersion-free pulses can remarkably reduce the defect absorption of terahertz waves and improve their transmittance by about 5.8 times.

Our approach meets the requirements of high-efficiency and high-precision simultaneously, also exhibiting good extensiveness and compatibility. This approach may also promote the development of $LiNbO_3$-based photonics and optoelectronics, nonlinear optics, topological photonics, as well as integrated quantum photonics and optical circuits, especially for THz-frequency chip-scale devices. Importantly, our approach is promising for precision machining of hard and brittle materials and for industrial-scale manufacturing applications due to its low cost, high flexibility, and good compatibility.

Funding

National Natural Science Foundation of China (11974192 and 62205158); the China Postdoctoral Science Foundation (2022M711709); Foundation of State Key Laboratory of Laser Interaction with Matter (SKLLIM2101); 111 Project (B23045); and Program for Changjiang Scholars and Innovative Research Team in University (IRT_13R29).

CRediT author statement

Xu Zhou: Conceptualization, Data curation, Formal analysis, Methodology, Software, Writing – original draft, Writing – review & editing. Yao Lu: Conceptualization, Data curation, Formal analysis, Methodology, Writing, Software, Writing – original draft, Writing – review & editing. Haibo Liu: Formal analysis, Resources, Writing – review & editing. Qiang Wu: Conceptualization, Formal analysis, Funding acquisition, Methodology, Project administration, Resources, Supervision, Writing – original draft, Writing – review & editing. Xitan Xu: Data curation, Writing – review & editing. Lu Chen: Formal analysis, Writing – review & editing. Zhixuan Li: Software, Writing – review & editing. Rui Wang: Resources, Writing – review & editing. Jin Guo: Funding acquisition, Writing – review & editing. Jingjun Xu: Funding acquisition, Resources, Writing – review & editing.

Declaration of competing interest

The authors declare that they have no known competing financial interests or personal relationships that could have appeared to influence the work reported in this paper.

Data availability

Data will be made available on request.

References

[1] K. Sengupta, T. Nagatsuma, D.M. Mittleman, Terahertz integrated electronic and hybrid electronic–photonic systems, Nature Electronics 1 (2018) 622–635.
[2] T. Nagatsuma, G. Ducournau, C.C. Renaud, Advances in terahertz communications accelerated by photonics, Nat. Photonics 10 (2016) 371–379.
[3] R. Wang, L. Xu, J. Wang, L. Sun, Y. Jiao, Y. Meng, S. Chen, C. Chang, C. Fan, Electric Fano resonance-based terahertz metasensors, Nanoscale 13 (2021) 18467–18472.
[4] M. Tonouchi, Cutting-edge terahertz technology, Nat. Photonics 1 (2007) 97–105.
[5] D.M. Mittleman, Twenty years of terahertz imaging, Opt Express 26 (2018) 9417–9431.
[6] M. Shalaby, M. Peccianti, Y. Ozturk, R. Morandotti, A magnetic non-reciprocal isolator for broadband terahertz operation, Nat. Commun. 4 (2013) 1558.
[7] R. Wang, Q. Wu, W. Cai, Q. Zhang, H. Xiong, B. Zhang, J. Qi, J. Yao, J. Xu, Broadband on-chip terahertz asymmetric waveguiding via phase-gradient metasurface, ACS Photonics 6 (2019) 1774–1779.
[8] A. Herter, A. Shams-Ansari, F.F. Settembrini, H.K. Warner, J. Faist, M. Lončar, I.-C. Benea-Chelmus, Terahertz waveform synthesis in integrated thin-film lithium niobate platform, Nat. Commun. 14 (2023) 11.
[9] J. Wang, S. Xia, R. Wang, R. Ma, Y. Lu, X. Zhang, D. Song, Q. Wu, R. Morandotti, J. Xu, Topologically tuned terahertz confinement in a nonlinear photonic chip, Light Sci. Appl. 11 (2022) 152.
[10] A. Boes, L. Chang, C. Langrock, M. Yu, M. Zhang, Q. Lin, M. Lončar, M. Fejer, J. Bowers, A. Mitchell, Lithium niobate photonics: unlocking the electromagnetic spectrum, Science 379 (2023) 40.
[11] M.G. Vazimali, S. Fathpour, Applications of thin-film lithium niobate in nonlinear integrated photonics, Adv. Photonics 4 (2022), 034001-034001.
[12] Y. Lu, Q. Zhang, Q. Wu, Z. Chen, X. Liu, J. Xu, Giant enhancement of THz-frequency optical nonlinearity by phonon polariton in ionic crystals, Nat. Commun. 12 (2021) 3183.
[13] H. Xiong, Y. Lu, Q. Wu, Z. Li, J. Qi, X. Xu, R. Ma, J. Xu, Topological Valley transport of terahertz phonon-polaritons in a $LiNbO_3$ chip, ACS Photonics 8 (2021) 2737–2745.
[14] G.K. Kitaeva, S. Kovalev, I. Naumova, A. Tuchak, P. Yakunin, Y. Huang, E. Mishina, A. Sigov, Terahertz wave generation in periodically poled lithium niobate crystals fabricated using two alternative techniques, Laser Phys. Lett. 10 (2013): 055404.
[15] Z. Ma, P. Li, S. Chen, X. Wu, Optical generation of strong-field terahertz radiation and its application in nonlinear terahertz metasurfaces, Nanophotonics 11 (2022) 1847–1862.
[16] B. Zhang, X. Wu, X. Wang, S. Li, J. Ma, G. Liao, Y. Li, J. Zhang, Efficient multicycle terahertz pulse generation based on the tilted pulse-front technique, Opt Lett. 47 (2022) 2678–2681.
[17] W. Shi, C. Li, H. Wang, Z. Wang, L. Yang, Quantitative detection of THz-ATR spectra of aqueous samples under strong-field terahertz wave, iScience 26 (2023): 105871.
[18] H. Wang, W. Shi, L. Hou, C. Li, Z. Wang, L. Yang, J. Cao, Quantitative analysis of aqueous biomolecular mixtures by THz spectroscopy based on high-power $LiNbO_3$ radiation source, Spectrochim. Acta Mol. Biomol. Spectrosc. 287 (2023): 122075.
[19] S. Kovalev, G.K. Kitaeva, N. Ilyin, I. Ilyakov, E. Mishina, A. Penin, A. Sigov, Nonlinear optical detection of terahertz-frequency radiation in crystals with periodic domain structure, Moscow Univ. Phys. Bull. vol. 66 (2011) 12–18.
[20] K. Luke, P. Kharel, C. Reimer, L. He, M. Loncar, M. Zhang, Wafer-scale low-loss lithium niobate photonic integrated circuits, Opt Express 28 (2020) 24452–24458.
[21] R. Wu, M. Wang, J. Xu, J. Qi, W. Chu, Z. Fang, J. Zhang, J. Zhou, L. Qiao, Z. Chai, Long low-loss-litium niobate on insulator waveguides with sub-nanometer surface roughness, Nanomaterials 8 (2018) 910.
[22] S. Liu, Y. Zheng, Z. Fang, X. Ye, Y. Cheng, X. Chen, Effective four-wave mixing in the lithium niobate on insulator microdisk by cascading quadratic processes, Opt Lett. 44 (2019) 1456–1459.
[23] B. Zhang, L. Wang, F. Chen, Recent advances in femtosecond laser processing of $LiNbO_3$ crystals for photonic applications, Laser Photon. Rev. 14 (2020): 1900407.
[24] G. Corrielli, A. Crespi, R. Osellame, Femtosecond laser micromachining for integrated quantum photonics, Nanophotonics 10 (2021) 3789–3812.
[25] Q. Li, Q. Wu, Y. Li, C. Zhang, Z. Jia, J. Yao, J. Sun, J. Xu, Femtosecond laser-induced periodic surface structures on lithium niobate crystal benefiting from sample heating, Photon. Res. 6 (2018) 789–793.
[26] Y. Li, Q. Wu, M. Yang, Q. Li, Z. Chen, C. Zhang, J. Sun, J. Yao, J. Xu, Uniform deep-subwavelength ripples produced on temperature controlled $LiNbO_3$:Fe crystal surface via femtosecond laser ablation, Appl. Surf. Sci. 478 (2019) 779–783.
[27] J. Imbrock, H. Hanafi, M. Ayoub, C. Denz, Local domain inversion in MgO-doped lithium niobate by pyroelectric field-assisted femtosecond laser lithography, Appl. Phys. Lett. 113 (2018): 252901.
[28] F. Chen, J.R. Vazquez de Aldana, Optical waveguides in crystalline dielectric materials produced by femtosecond- laser micromachining, Laser Photon. Rev. 8 (2014) 251–275.
[29] Y. Lu, Q. Wu, Q. Zhang, R. Wang, B. Zhang, W. Zhao, D. Zhang, H. Xiong, C. Yang, J. Qi, C. Pan, J. Xu, Time-resolved imaging of mode-conversion process of terahertz transients in subwavelength waveguides, Front. Phys. 14 (2019): 42502.
[30] Z. Fang, S. Haque, J. Lin, R. Wu, J. Zhang, M. Wang, J. Zhou, M. Rafa, T. Lu, Y. Cheng, Real-time electrical tuning of an optical spring on a monolithically integrated ultrahigh Q lithium nibote microresonator, Opt Lett. 44 (2019) 1214–1217.
[31] D. Wei, C. Wang, H. Wang, X. Hu, D. Wei, X. Fang, Y. Zhang, D. Wu, Y. Hue, J. Lie, S. Zhu, M. Xiao, Experimental demonstration of a three-dimensional lithium niobate nonlinear photonic crystal, Nat. Photonics 12 (2018) 596–600.
[32] D. Wei, C. Wang, X. Xu, H. Wang, Y. Hu, P. Chen, J. Li, Y. Zhu, C. Xin, X. Hu, Y. Zhang, D. Wu, J. Chu, S. Zhu, M. Xiao, Efficient nonlinear beam shaping in three-dimensional lithium niobate nonlinear photonic crystals, Nat. Commun. 10 (2019) 4193.
[33] J. Lv, Y. Cheng, J.R. Vazquez de Aldana, X. Hao, F. Chen, Femtosecond laser writing of optical-lattice-like cladding structures for three-dimensional waveguide beam splitters in $LiNbO_3$ crystal, J. Lightwave Technol. 34 (2016) 3587–3591.
[34] M. Heinrich, A. Szameit, F. Dreisow, S. Doering, J. Thomas, S. Nolte, A. Tuennermann, A. Ancona, Evanescent coupling in arrays of type II femtosecond laser-written waveguides in bulk x-cut lithium niobate, Appl. Phys. Lett. 93 (2008) 101111.
[35] S. Atzeni, A.S. Rab, G. Corrielli, E. Polino, M. Valeri, P. Mataloni, N. Spagnolo, A. Crespi, F. Sciarrino, R. Osellame, Integrated sources of entangled photons at the telecom wavelength in femtosecond-laser-written circuits, Optica 5 (2018) 311–314.
[36] D.A. Presti, V. Guarepi, F. Videla, A. Fasciszewski, G.A. Torchia, Intensity modulator fabricated in $LiNbO_3$ by femtosecond laser writing, Opt Laser. Eng. 111 (2018) 222–226.
[37] J. Lin, Y. Xu, Z. Fang, M. Wang, J. Song, N. Wang, L. Qiao, W. Fang, Y. Cheng, Fabrication of high-Q lithium niobate microresonators using femtosecond laser micromachining, Sci. Rep. 5 (2015) 8072.
[38] R. Stoian, M. Boyle, A. Thoss, A. Rosenfeld, G. Korn, I.V. Hertel, E.E.B. Campbell, Laser ablation of dielectrics with temporally shaped femtosecond pulses, Appl. Phys. Lett. 80 (2002) 353–355.

[39] N. Götte, T. Winkler, T. Meinl, T. Kusserow, B. Zielinski, C. Sarpe, A. Senftleben, H. Hillmer, T. Baumert, Temporal Airy pulses for controlled high aspect ratio nanomachining of dielectrics, Optica 3 (2016) 389–395.
[40] L. Jiang, A. Wang, B. Li, T. Cui, Y. Lu, Electrons dynamics control by shaping femtosecond laser pulses in micro/nanofabrication: modeling, method, measurement and application, Light Sci. Appl. 7 (2018) 17134.
[41] Q. Yang, X. Xie, J. Kang, H. Zhu, A. Guo, Q. Gao, Independent and continuous third-order dispersion compensation using a pair of prisms, High Power Laser Sci. Eng. 2 (2014).
[42] M. Stern, J.P. Heritage, E. Chase, Grating compensation of third-order fiber dispersion, IEEE J. Quant. Electron. 28 (1992) 2742–2748.
[43] S. Kane, J. Squier, Grism-pair stretcher–compressor system for simultaneous second-and third-order dispersion compensation in chirped-pulse amplification, J. Opt. Soc. Am. B 14 (1997) 661–665.
[44] M.F. Koldunov, A.A. Manenkov, I.L. Pokotilo, Mechanical damage in transparent solids caused by laser pulses of different durations, Quant. Electron. 32 (2002) 335–340.
[45] J. Han, Y. Li, C. He, Q. Zhang, R. Niu, L. Yang, G. Feng, Effects of laser plasma on damage in optical glass induced by pulsed lasers, Opt. Eng. 51 (2012) 121809.
[46] Y. Ito, R. Shinomoto, A. Otsu, K. Nagato, N. Sugita, Dynamics of pressure waves during femtosecond laser processing of glass, Opt Express 27 (2019) 29157–29166.
[47] B. Stuart, M. Feit, A. Rubenchik, B. Shore, R. Perry, Laser-induced damage in dielectrics with nanosecond to subpicosecond pulses, Phys. Rev. Lett. 74 (1995) 2248–2251.
[48] R.R. Gattass, E. Mazur, Femtosecond laser micromachining in transparent materials, Nat. Photonics 2 (2008) 219–225.
[49] Z. Chen, Q. Wu, M. Yang, B. Tang, J. Yao, R.A. Rupp, Y. Cao, J. Xu, Generation and evolution of plasma during femtosecond laser ablation of silicon in different ambient gases, Laser Part. Beams 31 (2013) 539–545.
[50] M. Sakakura, M. Terazima, Y. Shimotsuma, K. Miura, K. Hirao, Observation of pressure wave generated by focusing a femtosecond laser pulse inside a glass, Opt Express 15 (2007) 5674–5686.
[51] B. Rethfeld, D.S. Ivanov, M.E. Garcia, S.I. Anisimov, Modelling ultrafast laser ablation, J. Phys. D Appl. Phys. 50 (2017): 193001.
[52] J.P. Colombier, E. Audouard, R. Stoian, Laser pulses designed in time by adaptive hydrodynamic modeling for optimizing ultra-fast laser-metal interactions, Appl. Phys. Mater. Sci. Process 110 (2013) 723–729.
[53] F. Bourquard, T. Tite, A.-S. Loir, C. Donnet, F. Garrelie, Control of the graphite femtosecond ablation plume kinetics by temporal laser pulse shaping: effects on pulsed laser deposition of diamond-like carbon, J. Phys. Chem. C 118 (2014) 4377–4385.
[54] J. Hernandez-Rueda, J. Siegel, M. Galvan-Sosa, A.R. de la Cruz, M. Garcia-Lechuga, J. Solis, Controlling ablation mechanisms in sapphire by tuning the temporal shape of femtosecond laser pulses, J. Opt. Soc. Am. B 32 (2015) 150–156.